CONF-870839--6

KINETICS AND MECHANISM OF THERMAL AGING EMBRITTLEMENT OF DUPLEX STAINLESS STEELS*

H. M. Chung and O. K. Chopra

Materials and Components Technology Division
Argonne National Laboratory
Argonne, Illinois 60439

CONF-870839--6

DE88 002987

June 1987

The submitted manuscript has been authored by a contractor of the U. S. Government under contract No. W-31-109-ENG-38. Accordingly, the U. S. Government retains a nonexclusive, royalty-free license to publish or reproduce the published form of this contribution, or allow others to do so, for U. S. Government purposes.

DISCLAIMER

This report was prepared as an account of work sponsored by an agency of the United States Government. Neither the United States Government nor any agency thereof, nor any of their employees, makes any warranty, express or implied, or assumes any legal liability or responsibility for the accuracy, completeness, or usefulness of any information, apparatus, product, or process disclosed, or represents that its use would not infringe privately owned rights. Reference herein to any specific commercial product, process, or service by trade name, trademark, manufacturer, or otherwise does not necessarily constitute or imply its endorsement, recommendation, or favoring by the United States Government or any agency thereof. The views and opinions of authors expressed herein do not necessarily state or reflect those of the United States Government or any agency thereof.

To be presented at the Third International Symposium on Environmental Degradation of Materials in Nuclear Power Systems-Water Reactors, August 30-September 3, 1987, Traverse City, MI.

*Work supported by the Office of Nuclear Regulatory Research, U. S. Nuclear Regulatory Commission.

MASTER

DISTRIBUTION OF THIS DOCUMENT IS UNLIMITED

KINETICS AND MECHANISM OF THERMAL AGING EMBRITTLEMENT OF DUPLEX STAINLESS STEELS

H. M. Chung and O. K. Chopra

Materials and Components Technology Division
Argonne National Laboratory
Argonne, Illinois 60439

ABSTRACT

Microstructural characteristics of long-term-aged cast duplex stainless steel specimens from eight laboratory heats and an actual component from a commercial boiling water reactor have been investigated by SEM, TEM, SANS, and APFIM techniques. Three precipitate phases, i.e., Cr-rich α' and the Ni- and Si-rich G phase, and γ_2 austenite, have been identified in the ferrite matrix of the aged specimens. For CF-8 grade materials, $M_{23}C_6$ carbides were identified on the austenite-ferrite boundaries as well as in the ferrite matrix for aging at $\gtrsim$450°C. It has been shown that Si, C, and Mo contents are important factors that influence the kinetics of the G-phase precipitation. However, TEM and APFIM analyses indicate that the embrittlement for $\lesssim$400°C aging is primarily associated with Fe and Cr segregation in ferrite by spinodal decomposition. For extended aging, e.g., 6-8 yr at 350-400°C, large platelike α' formed by nucleation and growth from the structure produced by the spinodal decomposition. The Cr content appears to play an important role either to promote the platelike α' (high Cr content) or to suppress the α' in favor of γ_2 precipitation (low Cr). Approximate TTT diagrams for the spinodal, α', G, γ_2, and the in-ferrite $M_{23}C_6$ have been constructed for 250-450°C aging. Microstructural modifications associated with a 550°C reannealing and a subsequent toughness restoration are also discussed. It is shown that the toughness restoration is associated primarily with the dissolution of the Cr-rich region in ferrite.

New

INTRODUCTION

Cast duplex stainless steels, composed of dual phases of austenite and ferrite, are used extensively in the nuclear, oil, and chemical industries because of their superior strength, resistance to stress corrosion cracking, weldability, and soundness of casting. In nuclear reactors, designed to operate for ~40 yr at 280-330°C, cast stainless steels are used for primary cooling pipes, valves, and pump casings which are all vital for a safe operation of the reactors. It has long been known that ferritic stainless steels are susceptible to severe embrittlement when exposed to temperatures in the range of 300-500°C owing to the precipitation of the α' phase.[1-3] The potential for significant embrittlement of cast duplex stainless steels has been confirmed by recent studies on cast materials that were aged at temperatures between 300 and 450°C for times up to 70,000 h (~8 yr).[4-7] Until recently, embrittlement of the aged duplex stainless steel was attributed simply to Cr-rich α' precipitation, a mechanism similar to the "475°C embrittlement" of the ferritic stainless steels. However, despite the commonly accepted belief, earlier investigations by transmission electron microscopy (TEM) failed to identify the α' precipitation at the lower aging temperatures (i.e., $\lesssim$400°C) although mottled images of very fine scale (<3 nm) have been observed in reactor- and laboratory-aged specimens by weak-beam techniques.[8] For the lower temperatures, a spinodal decomposition of the ferrite rather than α' precipitation by nucleation and growth is predicted although exact temperatures for the spinodal boundary are not known for the ferrite phase in the cast duplex stainless steels. For these duplex stainless steels, the low-temperature spinodal decomposition and the subsequent precipitation of the α' phase by nucleation and growth that is possible during a long-term aging have not been characterized.

In addition to the spinodal decomposition, it has been reported that the structure of the aged duplex stainless steels is further complicated by a number of other deleterious phases that precipitate simultaneously, i.e., Ni- and Si-rich G phase that is $\lesssim$10 nm in size,[8-11] an unidentified phase that precipitates on dislocations in ferrite,[8] and carbides on the austenite-ferrite phase boundries.[8] A review of available information on these phases shows that a large variation in the precipitation kinetics among different heats is common even though the ferrite content and nominal chemical compositions are comparable. Similarly, a large variation in mechanical properties is also common for similar aging conditions. Thus, it seems important to identify the critical factors in heat treatment or chemical composition that influence the kinetics of these precipitations. In the present work, microstructural characterization in a complementary manner by a combination of advanced metallographic techniques of the APFIM, small-angle neutron scattering (SANS), and TEM appeared suitable. The objective of this study was twofold: to elucidate the embrittlement mechanisms and to identify the critical factors that control the kinetics of the microstructural evolution.

EXPERIMENTAL PROCEDURES

Materials and Aging

Specimens from four heats of cast duplex stainless steels have been obtained from the Georg Fischer Co. of Switzerland after aging for 1000 to 70,000 h at 400, 350, and 300°C. Also obtained for the microstructural investigation was the pump cover from the KRB reactor, a boiling-water reactor in Gundremingen, West Germany. The reactor pump cover had been in service for ~12 yr. Several additional experimental and commercial heats were aged at

280-450°C in this laboratory and were examined after 1000 to 10,000 h of aging.[12] Chemical compositions of the examined specimens are listed in Table I.

TEM

Thin-foil specimens for TEM examination were jet-thinned in an electrolytic solution of 19% ethanol, 27% butyl cellosolve, 17% perchloric acid, and 37% water. During jet-thinning, the solution was maintained at -20 to -30°C. TEM examination was conducted in a JEOL 100CX-II scanning transmission electron microscope or an AEI-EM7 high-voltage electron microscope (HVEM), which were operated at 0.1 and 1 MeV, respectively. The camera lengths of the microscopes were calibrated independently. Reflections from the matrix were used as standards to find an exact camera length for each diffraction pattern.

APFIM

Characterization by APFIM were conducted with the FIM 100 atom probe at Oxford University in England, and details of the procedures have been reported elsewhere.[13] Base pressures of the probe were typically 5 x 10^{-11} mbar. Images were obtained using neon gas at ~100 K. Mass spectra were obtained at -208 or -173°C, using voltage pulses, with a pulse-to-standing voltage ratio of 15%.

SANS

The SANS experiments were conducted with the 30-meter instrument at the National Center for Small-Angle Scattering at Oak Ridge National Laboratory. Details of the measurements have been reported elsewhere.[14] A monochromatic neutron beam of 0.475-nm wavelength impinged on the aged specimens and the intensity of the scattered neutrons was measured by a detector as a function of the scattering angle. The distance between the detector and specimen was

2.0-18.9 m which allowed the scattering vector (Q) a range of 0.0028-0.21 inverse Angstrom. The scattering vector is defined as

$$Q = \frac{4\pi}{\lambda} \sin \theta,$$

where λ is the wavelength of the neutron and θ is the scattering angle. Because of the two-meter limit in the detector-specimen distance, a lower limit was expected for the size of detectable precipitates. Information on the size and distribution of the scattering centers (precipitates) was obtained from the well-known Guinier approximation for spherical inhomogenities.[15]

RESULTS AND DISCUSSION

Characterization of the aged specimens by TEM, SANS, and APFIM showed the spinodal decomposition and four types of precipitates in the ferrite phase, i.e., α', G, γ_2 austenite, and spherical $M_{23}C_6$. TEM examination also revealed $M_{23}C_6$ carbides for high-carbon CF-8 or CF-8M grade materials on or near the austenite-ferrite phase boundaries.

G Phase

Several morphologies and selected-area diffraction (SAD) patterns of the Ni- and Si-rich G-phase precipitates are shown in Fig. 1. The dark-field images of Figs. 1A to 1C, produced from $(333)_G$ reflections, are indicative, respectively, of an early, intermediate, and extensive stage of the G-phase precipitation. The G-phase precipitates initially in a heterogeneous manner on or near dislocations (Fig. 1A) and eventually in a homogeneous manner in the ferrite matrix (Fig. 1C). A comparison of the two figures illustrates the effect of the aging time (i.e., 10,000 vs 70,000 h) at 400°C for heat 280. In the saturated state of Fig. 1C, it can be seen that the precipitates on the dislocations are a few times larger than those away from the dislocations (i.e., ~5 vs ~10 nm).

Orientations of Figs. 1A and 1C are identical (011) zones of ferrite as shown in the corresponding SAD patterns of Figs. 1D and 1E. A comparison of the two patterns shows that the weak reflection denoted by the arrow in Fig. 1D is indeed the relatively strong $(3\bar{3}3)_G$ reflection of the G phase in Fig. 1E. The angle between the $(3\bar{3}3)_G$ and the $(0\bar{1}1)_{\alpha'}$, or the $(0\bar{4}4)_G$, is ~35.4°. Other precipitate reflections in the print are too weak to be visible. Similar SAD patterns containing the $(333)_G$ reflections of the G phase and dark-field images were also observed in specimens after aging at 300°C for 70,000 h. Thus, the unidentified phase that was observed previously in association with dislocations[8] is indeed the early-stage G phase which precipitated heterogeneously on the dislocations. It seems that the dislocations act as preferential nucleation sites for G-phase precipitation at aging temperatures of 280-400°C. The irradiation-induced precipitation of the G phase reported by Gelles and Thomas[16] indicates that the undersize solute Si tends to interact preferentially with irradiation-induced defects. In this respect, Si interaction with another type of defect, i.e., dislocations, under thermal aging conditions, appears quite possible.

The kinetics of the G-phase precipitation was significantly faster for heat 278 than for heat 280 at the 300°C aging temperature. Relative kinetics for the 400°C aging, deduced from TEM examination, were similar. ~~i.e., the kinetics for heat 278 were significantly faster than those for heat 280.~~ A quantitative comparison of the precipitate densities for the two heats was obtained by means of SANS experiments (see below); the results confirmed the TEM observation. Similar results for 400°C, 10,000 h aging were also observed for heats 60 and 51, which, except for the carbon level, had comparable chemical and ferrite contents. For the high-carbon (CF-8 grade) heat 60 specimens, G-phase precipitation was significantly more extensive than for the low-carbon (CF-3 grade) heat 51. The carbon content of heat 278 is also significantly higher than heat 280 (Table I). A comparison of the differences in the chemical contents of heats 278 and 280 and the chemical contents[9,11] reported for the G phase indicates that the carbon level is the only factor that is consistent with the faster kinetics of the G-phase precipitation for heats 278 and 60 (relative to heats 280 and 51, respectively). This observation is corroborated further from the following analysis regarding the relative distribution of the G phase and spherical $M_{23}C_6$ in ferrite.

$M_{23}C_6$ in Ferrite

For the aging temperature of 450°C, the G phase as well as spherical $M_{23}C_6$ carbides precipitated in the ferrite matrix for high-carbon materials. Figure 2 shows a bright-field image and a SAD pattern of an austenite-ferrite boundary of a heat 60 specimen aged at 450°C for 3000 h. The figure also shows dark-field images of the G phase and $M_{23}C_6$ carbides in which the size and distribution of the two phases are more clearly visible. In addition to the phase boundary carbides, smaller spherical carbides, ~60 nm in diameter, are observed in the ferrite matrix in Fig. 2B. The G-phase precipitates revealed in the dark-field image of Fig. 2B are ~10 to 20 nm in size, several times larger than those formed at 400°C. Also visible in the figures are relatively large G-phase precipitates which apparently formed on the preferential nucleation sites near the phase boundary $M_{23}C_6$ carbides. A systematic comparison of a number of dark-field images obtained with the carbide and G-phase reflections showed that the G-phase precipitation was preferentially associated with the spherical in-ferrite carbides as well. This is illustrated in Figs. 2B and 2C, in which relatively denser G-phase precipitates are observed near the in-ferrite carbide positions (denoted by circles). The above observations on the relative distribution of carbides and G phase indicate a role of carbon atoms or carbide nuclei on G-phase precipitation. Carbon has been reported as a constituent of the G phase from APFIM analyses by Bentley et al.[11] Therefore, local clusters of carbon would be expected to promote the G-phase precipitation. The indication that carbon promotes the G-phase precipitation is also consistent with the SANS analysis of G-phase distributions in heats 278 and 280 (see below).

Precipitation of the spherical carbides in the ferrite matrix indicates that embrittlement data from the high-carbon CF-8 grade steels produced after aging at 450°C cannot be extrapolated to reactor operating temperatures.

$M_{23}C_6$ on Austenite-Ferrite Boundary

$M_{23}C_6$ precipitation on austenite-ferrite boundaries in CF-8 materials has been reported previously.[8] Figure 3 shows a comparison of several morphologies of the carbides for CF-8 and CF-8M materials. In contrast to the carbide precipitates on the phase boundary (e.g., Figs. 2 and 3A), an extensive aging (400°C, 70,000 h) of heat 278 (carbon content 0.038 wt %) produced intragranular $M_{23}C_6$ in austenite near the austenite-ferrite boundary (Fig. 3B). The carbides showed a cube-on-cube orientation and a predominance of {111} faces. However, no carbides were observed for the similar heat 280 for a similar aging condition. The difference on the two heats may be attributed to the higher carbon as well as the higher Ni contents for heat 278 (Table I). The effect of the latter promoting the $M_{23}C_6$ precipitation in austenite has been reported by Kegg and Silcock.[19] $M_{23}C_6$ in the austenite similar to Fig. 3B but with different morphologies has been also observed for CF-8M graded after aging at 400°C for 10,000 h (Figs. 3C and 3D). It appears that, even for the 400°C aging, precipitation of either the relatively large $M_{23}C_6$

in austenite or the small carbides in ferrite (such as Fig. 2B) cannot be ruled under an extensive aging condition for high-carbon CF-8 or CF-8M materials. The effects of the phase boundary carbides on weakening the boundaries and lowering the impact toughness have been reported elsewhere.[8,12] However, information on the effects on the stress corrosion susceptibility is not available.

Mo Content and G-Phase Kinetics

In the ferrite grain at the left-hand side of the bright-field image of Fig. 3D, a high density of G-phase precipitates, ~5 to 8 nm in size, are visible. The G-phase density for heat 286 (aged at 400°C for 10,000 h) is comparable with that of the CF-8 grade aged at 400°C for 70,000 h. Apparently, in CF-8M steels, Mo atoms accelerate the G-phase precipitation, a phase that is reported to contain ~15 at. % Mo.[11] It appears that the faster embrittlement of the CF-8M materials[4] is primarily as a result of the faster G-phase precipitation in ferrite.

α' - Spinodal Decomposition

Chromium-rich α' precipitates in the ferrite could not be detected by TEM for specimens aged for a short-term at $\lesssim$400°C. However, mottled morphology images characteristic of a spinodal decomposition could be observed in the ferrite of specimens aged at 300°C for 70,000 h or 400°C for 10,000 h. Figure 4A shows that a mottled image was observed in the ferrite but not in the austenite.

Apparently, the mottled images were produced as a result of nonuniform oxidation during jet-thinning in the ferrite grain over extremely small distances of a nonuniform distribution of Fe and Cr. It is not clear whether the Fe- or Cr-enriched region was oxidized preferentially. However, it has been reported previously that thin layers of Cr_2O_3 are formed on the Cr-rich region, creating the mottled morphology.[17] When the Fe and Cr concentrations are uniform, no mottled oxide layers will be formed, e.g., the austenite grain of Fig. 4A. To confirm the premise that the mottled morphologies were produced as a result of the spinodal decomposition, several specimens aged under different conditions were chosen for analysis by APFIM. The results were compared with TEM observations. The APFIM profiles for Cr, Ni, and Fe shown in Fig. 4C were obtained for the ferrite phase of a heat 280 specimen after aging at 300°C for 70,000 h. A corresponding TEM image is shown in Fig. 4B.

It can be seen, in Fig. 4C for example, that a Cr-rich region shows a relative depletion of Fe and Ni, and vice versa. This one-to-one correspondence between the Cr enrichment and the Fe and Ni depletion shows that the elemental fluctuations are not random, but occur as a result of a spinodal decomposition similar to that of the binary Fe-Cr ferritic alloy. The size of the black oxide dots, determined from the TEM image of Fig. 4B, is ~2 nm. This is in good agreement with the thickness of the Cr-depleted region, which is estimated from Fig. 4C to be ~1.5-2 nm. Likewise, from Fig. 4B, the distance between the black oxide dots is estimated to be ~5-6 nm. This is also consistent with the separation of the Cr-rich regions in Fig. 4C. Thus, it seems that the Fe and Cr profiles obtained by APFIM and the mottled images obtained by TEM are consistent with the interpretation that the black oxide dots are associated with the local segregatgion of Fe and Cr by spinodal decomposition.

α' - Nucleation and Growth During Extended Aging

For most of the specimens examined, only spinodal decomposition was evident for aging temperatures $\lesssim$400°C. However, large platelike α' precipitates were observed in some long-term-aged specimens, i.e., heat 280N, aged at

350°C for 56,000 h, and heat 280, aged at 400°C for 70,000 h (Ref. 12C). The morphology, shown in Fig. 5, is similar to those reported by Lagneborg[17] and Blackburn and Nutting[18] for Fe-Cr alloys for higher temperatures. Trace analysis of the plate-shaped α' showed $\{100\}_\alpha$ habit plane, which is also in agreement with Refs. 17 and 18. The large platelike α' was observed neither for heat 280, aged at 350°C for 70,000 h, nor for heat 278, aged for 70,000 h at 350 and 400°C.

The precipitation of the larger platelike α' is apparently deleterious to the toughness of the material more than any other precipitates. The more rapid precipitation of the large platelike α' in heat 280N (compared to heat 280) appears to have resulted in the faster embrittlement of heat 280N than heat 280.[4] However, the mechanism that leads to a faster precipitation of the large platelike α' in heat 280N or why they are not formed in heat 278 after a similar aging is not understood at this time. In Fig. 6, reported data for the onset of the platelike α' precipitation for several ferritic alloys are plotted and compared with the approximate results obtained in this study. Solomon and Levinson[20] reported an order of magnitude faster precipitation for a duplex steel (U50) compared to ferritc steels. The estimated result for heat 280N (denoted by the number 1 in Fig. 6) is in reasonable agreement with an extrapolation that is based on the result of Solomon and Levinson (denoted by number 5) and on an activation energy of 48 kcal/mol (i.e., the activation energy of Cr diffusion in Fe-25Cr alloy[21]). According to the extrapolation, the large platelike α' is predicted to precipitate after ~40 yr at ~320°C. However, the uncertainty limit is unacceptably too large, and a further investigation is necessary to resolve this important question.

γ_2 Precipitation in Ferrite

γ_2 (austenite) precipitation in ferrite of aged specimens was observed in heat 278, aged at 400°C for 70,000 h. For other specimiens, no γ_2 was observed even for the similar long-term aging conditions. For the extensively aged specimens of heats 280N or 280 in which the platelike α' was observed, γ_2 was conspicuously absent. It is possible that the relatively higher Cr content in the two heats resulted in the platelike α' precipitates, and as a consequence, formation of the γ_2 was suppressed. Relative kinetics and interrelationship of the γ_2 and α' precipitation are, however, not well understood at present and a further study is needed.

Figure 7 shows the morphology and diffraction characteristics of the γ_2 which was observed in the heat 278 specimen (aged at 400°C for 70,000 h). Reflections of the γ_2 (Fig. 7B) were streaked, indicating a sheet-like morphology. Effects of γ_2 on the mechanical properties are not clear. For heat 278, the extent of the γ_2 precipitation was yet very small after the 400°C, 70,000 h aging.

Characterization by SANS

Specimens from the laboratory-aged heats 278 and 280 were selected and analyzed with the SANS technique to provide quantitative information on the size and distribution of precipitates. Details of the analysis have been reported in Ref. 12B. The results of the SANS analysis were compared with the results of TEM analysis. The neutron-scattering characteristics of the two heats are shown in Fig. 8 for aging at 400°C for 10,000 and 70,000 h. The scattering characteristics for the longer aging for the two heats are similar except that the intensity is higher for the heat 280 specimen which had a ferrite content ~2.5 times higher than that of the heat 278 specimen (i.e., 38 vs 15%). When the two curves were normalized with respect to the ferrite content, the scattering characteristics were, in fact, identical. This means that the scattering centers are precipitates contained in the ferrite phase, not in the austenite phase.

From the Guinier transformation[15] of Figs. 8A and 8B, size distributions were determined and plotted in Fig. 8C. The curves for heat 278 show that the size of the precipitates increases from ~1.6 nm for 10,000 h of aging to ~5.5 nm for 70,000 h of aging. This shows an Ostwald ripening of the precipitates. The size distribution of the scattering centers for the heat 280 was virtually identical to heat 278, except for the 400°C, 10,000 h aging in which the density of the scattering centers was negligible. To identify the nature of the scattering centers, the results were compared with the TEM observations. A comparison of the SANS size distribution (Fig. 8C) and the TEM image (Fig. 1C) for the 400°C, 70,000 h aging of heat 280 shows that the SANS distribution is nearly identical to the G-phase distribution i.e., a size range of 3-10 nm with the most populous size being 5-6 nm, with the exception of a few precipitates as large as ~15 nm on the dislocations. Apparently, the relatively smaller number of the large precipitates on the dislocations could not be detected by SANS because of a low-volume fraction. Likewise, the negligible intensity shown in Fig. 8C for the 400°C, 10,000 h aging of the heat 280 specimen is consistent with the TEM microstructure of Fig. 1A in which the G-phase density in the ferrite phase is negligible except for the decoration of dislocations. Relative intensities for the 400°C, 10,000 h aging for the two heats are also consistent with the TEM observation on the relative kinetics of the G-phase precipitation, i.e., a faster precipitation for a higher carbon content. Thus, the above comparisons of the SANS and TEM results appear to show that the scattering centers depicted in Fig. 8 are indeed the G-phase precipitates.

The spinodal decomposition of the ferrite phase has been observed for all specimens aged at 400°C for $\gtrsim$3000 h. Therefore, Fe and Cr segregation is expected in specimens of heats 278 and 280 aged at 400°C for 10,000 h. Thus, the difference in the scattering characteristics shown in Fig. 8C cannot be explained on the basis of the spinodal decomposition or the Cr-rich α' precipitation. Likewise, the nearly identical scattering curves for the 400°C, 70,000 h aging do not indicate a peak corresponding to the size of the Cr-rich region. For the present SANS experiments, the minimum distance between the specimen and detector was ~2 m. This would limit the maximum angle of detection of the scattered neutrons, and hence, the α' precipitates of very fine size that would scatter neutrons in larger angles (i.e., larger scattering vector) may not have been detected.

Toughness Recovery by 550°C Annealing

Long-term-aged specimens from several heats were annealed at 550°C for 1 h to determine the extent of toughness recovery affected by high-temperature annealing. Room temperature Charpy-impact energies for the KRB pump cover obtained before and after the annealing at 550°C were ~110 and 220 J/cm^2, respectively. Ferrite phase hardness measurements also demonstrated a virtual restoration of the toughness after the 550°C anneal for all the long-term-aged specimens (Table II).

To identify the mechanism of the toughness recovery, microstructural evolution during the 550°C anneal was characterized, either after cooldown of the specimens or in-situ in the HVEM hot stage. The in-situ observation of the large platelike α' was shown in Fig. 5. The α' dissolved at 510-520°C within one minute in the HVEM. Figure 9 shows similar results for the spinodal decomposition and the G phase. In Fig. 9A, a mottled image from the spinodal decomposition in the KRB pump cover is visible with a few dislocations. After the 550°C, 1 h anneal and an impact fracture, the mottled image is absent, but a high density of dislocations are visible, indicating an easy dislocation movement during the impact test (Fig. 9B). A comparison of Figs. 9C and 9D shows that the G phase is largely intact. It is therefore concluded that the toughness recovery is primarily due to the dissolution of the Cr-rich regions in the ferrite.

CONCLUSIONS

1. Five metallurgical processes that contribute to the thermal-aging embrittlement of the ferrite phase of the duplex cast stainless steels have been identified for 280-450°C, i.e., spinodal decomposition, nucleation and growth of α', G, γ_2, and spherical $M_{23}C_6$ carbides. Approximate TTT diagrams for the processes are shown in Fig. 10.
2. For high-carbon CF-8 grade steels, $M_{23}C_6$ precipitation on the austenite-ferrite boundary weakens the boundary and decreases the material toughness. Aging data obtained for $\gtrsim$400°C for the CF-8 grade are probably not adequate for extrapolation to lower temperatures.
3. The primary embrittlement mechanism of the aged cast stainless steels is the formation of Cr-rich α'. For aging temperatures $\lesssim$400°C, α' is formed initally by spinodal decomposition of the ferrite matrix to produce Fe and Cr segregation on a very fine scale, $\lesssim$3 nm. For long-term aging, platelike α' precipitates a few orders of magnitude larger are formed out of the initial structure of spinodal decomposition. The kinetics of this process, however, are not well understood at this time. The embrittling effects of the Fe and Cr segregation by the spinodal decomposition can be mitigated by annealing the material at 550°C for 1 h. The toughness is virtually restored by the annealing.

4. Carbon and Mo atoms accelerate the precipitation of the G phase. For short-term aging, the G phase preferentially precipitates on dislocations, followed by a homogeneous precipitation in the ferrite matrix. Subsequently, upon long-term aging, an Ostwald ripening takes place.
5. Lower levels of Mo, Si, C, and probably N and Cr, in the cast duplex stainless steels, as well as a smaller ferrite content, will be benefical for a better resistance to the thermal-aging embrittlement.

ACKNOWLEDGMENT

This work was supported by the Office of the Nuclear Regulatory Research, U. S. Nuclear Regulatory Commission. The authors are grateful to A. Tratuwein, of the Georg Fischer Company of Switzerland, for his efforts in making the long-term-aged specimens available for this work, and to R. A. Conner, Jr. and G. Dragel for their experimental contributions. The authors also wish to thank J. Muscara, W. J. Shack, and T. F. Kassner for helpful discussions.

REFERENCES

1. H. D. Solomon and T. M. Devine, "Influence of Microstructure on the Mechanical Properties and Localized Corrosion of a Duplex Stainless Steel," in Micon 78: Optimization of Processing, Properties, and Service Performance through Microstructural Control, Abrams, Maniar, Nail and Solomon, eds., ASTM STP 672, p. 430 (1979).
2. P. J. Grobner, Metall. Trans. 4, 251 (1973).
3. T. J. Nichol, A. Datta, and G. Aggen, Metall. Trans. 11A, 573 (1980).
4. A. Trautwein and W. Gysel, "Influence of Long Time Aging of CF-8 and CF-8M Cast Steel at Temperatures Betweeen 300 and 500°C on the Impact

Toughness and the Structure Properties," Spectrum, Technische Mitteilungen aus dem GF Konzern 5 (May 1981); also in Stainless Steel Castings, V. G. Behal and A. S. Melilli, eds., ASTM STM 756, p. 165 (1982).

5. G. Baudry and C. Pichard, "Evolution During Long Holding Times at 300 and 450°C of the Mechanical Properties of Austeno-Ferritic Steel Castings and Welded Joints Used in Pressurized Water Nuclear Reactors," in Troisieme Congres National sur la Technologie des Appareils a Bression, Vol. 2, Materiaux, A.F.I.A.P., p. 673 (1980).
6. E. I. Landerman and W. H. Bamford, "Fracture Toughness and Fatigue Characteristics of Centrifugally Cast Type 316 Stainless Steel Pipe after Simulated Thermal Service Conditions; Ductility, and Toughness Considerations in Elevated Temperature Service," Am. Soc. Mech. Eng. MPC-8, p. 99 (1978).
7. G. Slama, P. Petrequin, and Magep, "Effect of Aging on Mechanical Properties of Austenitic Stainless Steel Castings and Welds," Presented at SMIRT Post-Conference Seminar 6, Assuring Structural Integrity of Steel Reactor Pressure Boundary Components, August 29-30, 1983, Monterey, CA.
8. H. M. Chung and O. K. Chopra, "Microstructure of Cast Duplex Stainless Steel after Long-Term Aging," in Proc. Second Int. Symp. on Environmental Degradation of Materials in Nuclear Power Systems - Water Reactors, September 9-12, 1985, Monterey, CA, American Nuclear Society, LaGrange Park, IL, pp. 287-292 (1986).
9. M. Vrimat, R. Cozar, and Y. Mayzaud, Scripta Metal. 20, 1101 (1986).
10. M. K. Miller, J. Bentley, S. S. Brenner, and J. A. Spitznagel, J. de Phys. (Paris), Colloq. 45, C9-385 (1984).

11. J. Bentley, M. K. Miller, S. S. Brenner, and J. A. Spitznagel, in Proc. 43rd Annual Meeting of the Electron Microscopy Society of America, G. W. Bailey, ed., San Fransisco Press, pp. 328-329 (1985).

12. O. K. Chopra and H. M. Chung, Long-Term Embrittlement of Cast Duplex Stainless Steels in LWR Systems: Semiannual Reports, Argonne National Laboratory, (A) ANL-86-3, October 1984-September 1985, (B) ANL-86-54, October 1985-March 1986, (C) ANL-87-16, April-September 1986.

13. T. J. Godfrey and G. D. W. Smith, "The Atom Probe Analysis of a Cast Duplex Stainless Steel," presented at the 33rd International Field Emission Symposium, July 7-11, 1986, West Berlin, Germany.

14. J. E. Epperson, J. S. Lin, and S. Spooner, "The Fine Scale Microstructure in Cast and Aged Duplex Stainless Steels Investigated by Small Angle Neutron Scattering," presented at the 13th International Symposium on Effects of Radiation on Materials, June 23-25, 1986, Seattle, Washington.

15. "Treatise on Materials Science and Technology," Vol. 15, "Neutron Scattering," ed. G. Kostorz, Academic Press, 1979.

16. D. S. Gelles and L. E. Thomas, "Effects of Neutron Irradiation on Microstructure in Commercial and Experimental Ferritic Alloys," Topical Conf. on Ferritic Alloys for Use in Nuclear Energy Technologies, June 19-23, 1983, Snowbird, UT.

17. R. Lagneborg, Trans. Am. Soc. Met. 60, 67 (1967).

18. M. J. Blackburn and J. Nutting, J. Iron Steel Inst. 202, 610 (1964).

19. G. R. Kegg and J. M. Silcock, Metal Science J. 6, 47 (1972).

20. H. D. Solomon and L. M. Levinson, Acta Metal. 26, 429 (1978).

21. H. W. Paxton and T. Kunitake, Trans. AIME 218, 1003 (1960).

TABLE I. Chemical Compositions of Cast Duplex Stainless Steels Used for Studies of Aging Embrittlement

Heat No.	Grade	Composition (wt %)									Ferrite Content (%)
		Mn	Si	Mo	Cr	Ni	P	S	N	C	
280N[a]	CF-8	0.50	1.37	0.25	21.60	8.00	0.015	0.006	0.029	0.028	38
280[b]	CF-8	0.50	1.37	0.25	21.60	8.00	0.015	0.006	0.029	0.028	38
278	CF-8	0.28	1.00	0.13	20.20	8.27	0.008	0.019	0.027	0.038	15
286	CF-8M	0.40	1.33	2.44	20.20	9.13	0.044	0.015	0.063	0.072	22
60	CF-8	0.71	1.01	0.26	21.02	8.07	-	-	0.050	0.070	21
51	CF-3	0.66	1.06	0.28	20.36	8.69	-	-	0.050	0.020	18
KRB Reactor[c] Pump	CF-8	0.31	1.17	0.17	21.99	8.03	-	-	0.038	0.062	34

[a] Production heat, solution annealed at 1010°C for 12 h and water-quenched.

[b] Heat 280N heat treated additionally, i.e., solution annealed at 1050°C for 4 h and water-quenched.

[c] A boiling-water reactor in Gundremingen, West Germany. The pump cover was obtained for tests after ~12 yr of service.

New

TABLE II. Results of Vickers Hardness Measurements in Ferrite Phase of Long-Term-Aged Cast Stainless Steels before and after the 550°C, 1 h Annealing[a]

Heat	Specimen Number	Aging Temp. (°C)	Aging Time (h)	Hardness (As-Aged)	Hardness after 550°C Anneal
278	B8	350	70,000	373 ± 10	218 ± 10
278	C8	400	70,000	383 ± 6	-
280	B8	350	70,000	469 ± 16	215 ± 8
280	C8	400	70,000	437 ± 15	240 ± 10
286	C6	400	10,000	-	-
280N	603E16	350	56,000	493 ± 15	234 ± 6
280N	604E16	350	56,000	445 ± 8	232 ± 12
KRB Reactor Pump		280	~12 yr service	287 ± 10	210 ± 7

[a] Annealed in air and air cooled.

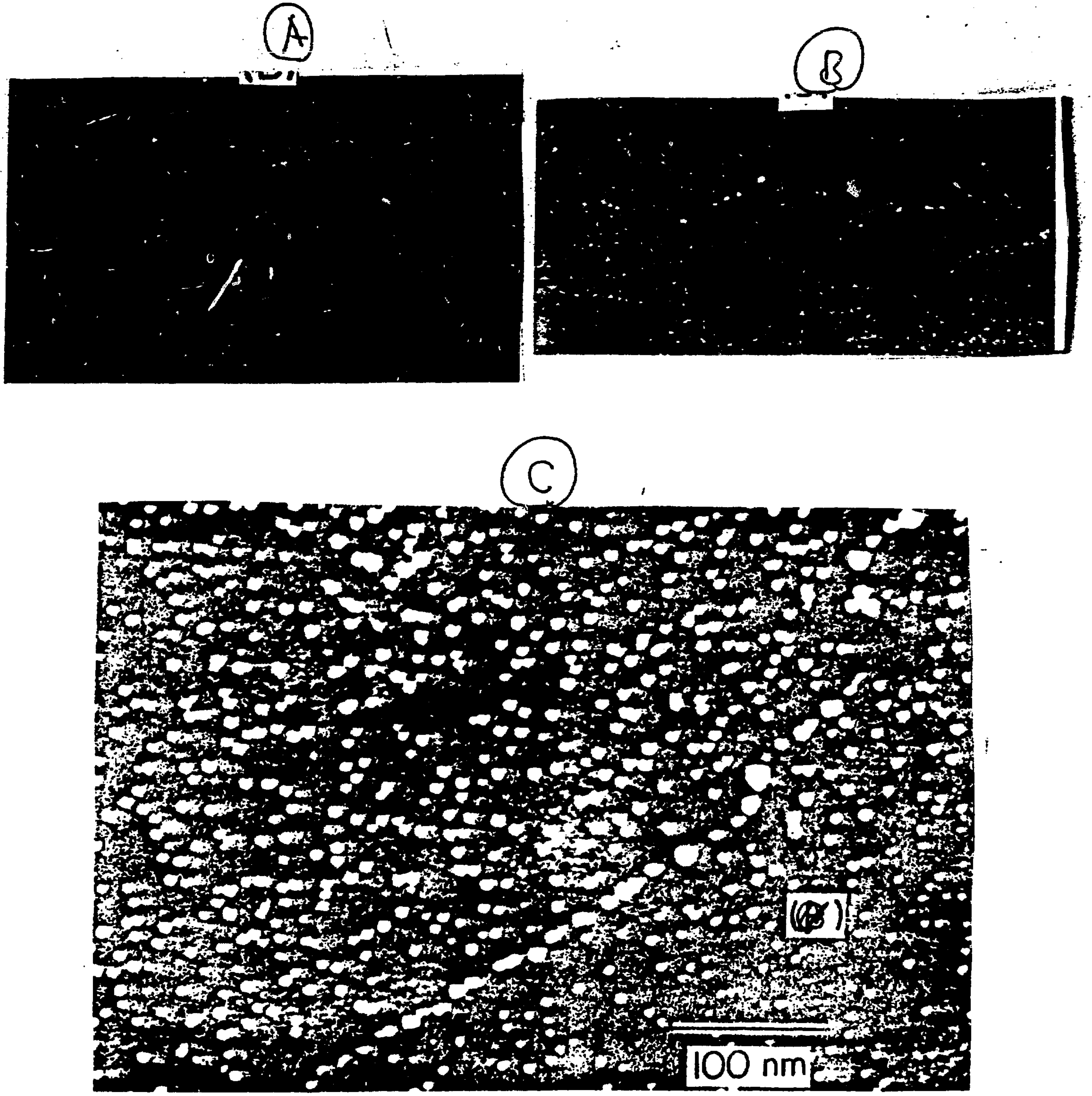

Fig. 1. Dark-Field Images Showing the G Phase Size and Distribution in Specimens of (A) Heat 280, Aged at 400°C for 10,000 h; (B) Heat 278, Aged at 300°C for 70,000 h; (C) Heat 280, Aged at 400°C for 70,000 h; (D) SAD Pattern of (A); and (E) SAD Pattern of (C).

①

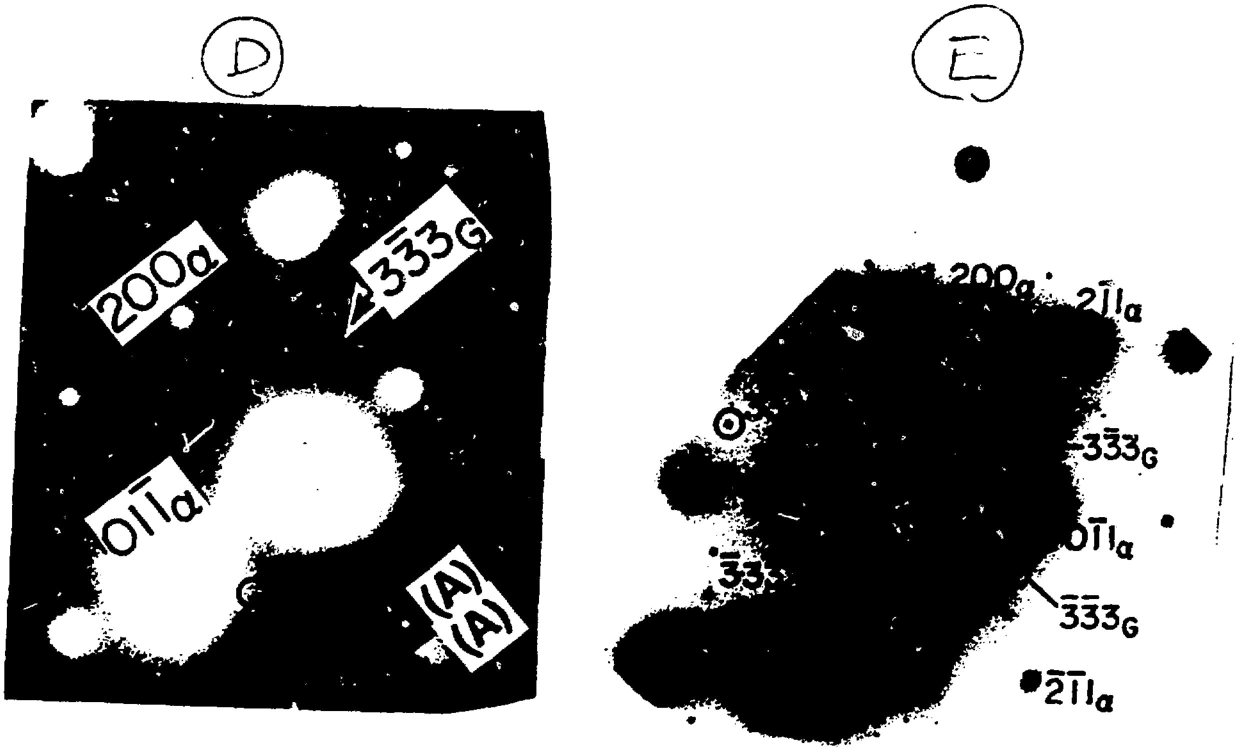

Fig. 1. (Contd.)

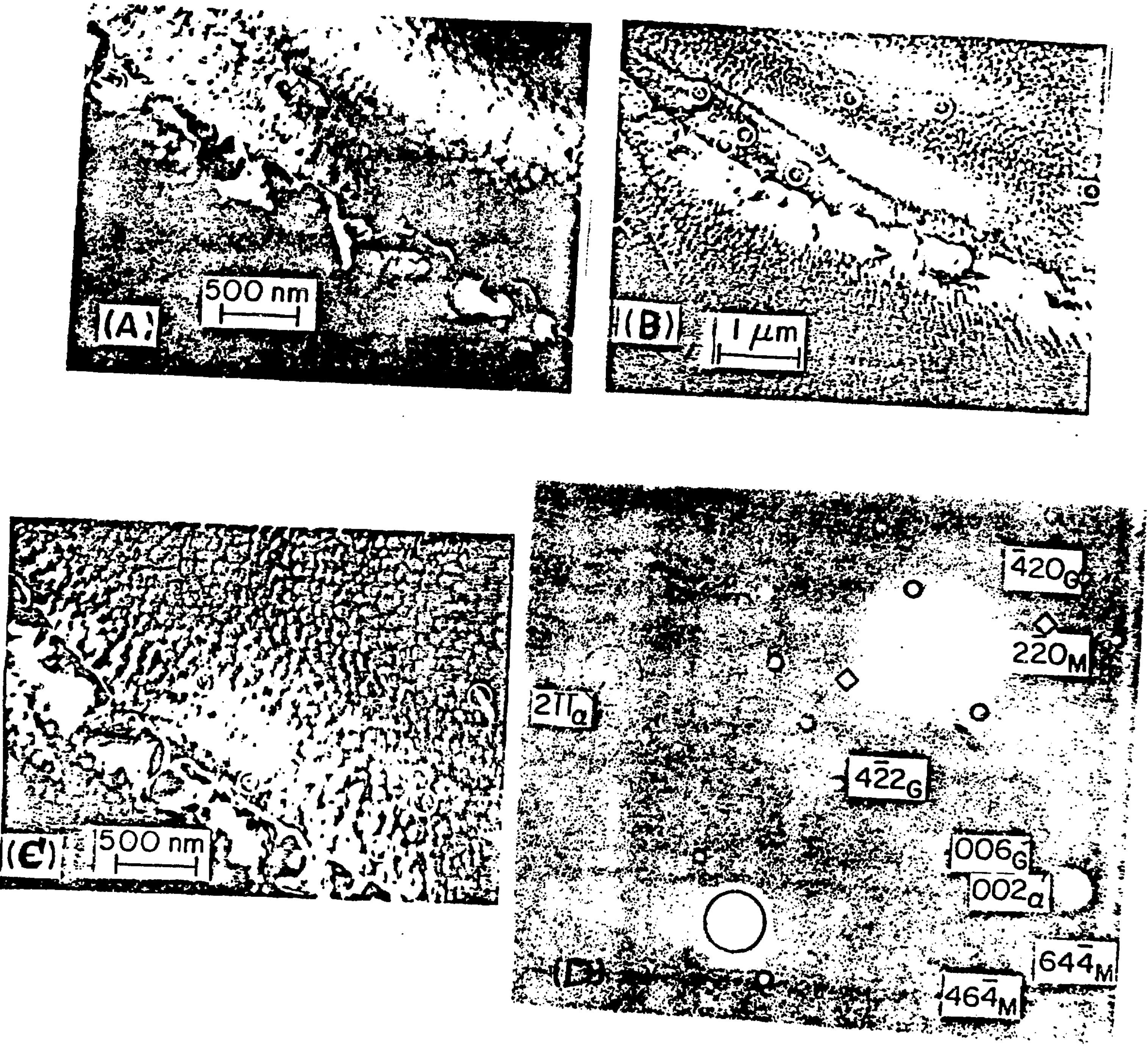

Fig. 2. TEM Images of Heat 60 after Aging at 450°C for 3000 h. (A) Bright-field image of austenite-ferrite boundary; (B) dark-field image of $M_{23}C_6$ in the ferrite and on the austenite-ferrite boundary; (C) dark-field image of G phase; and (D) SAD pattern of (A).

③

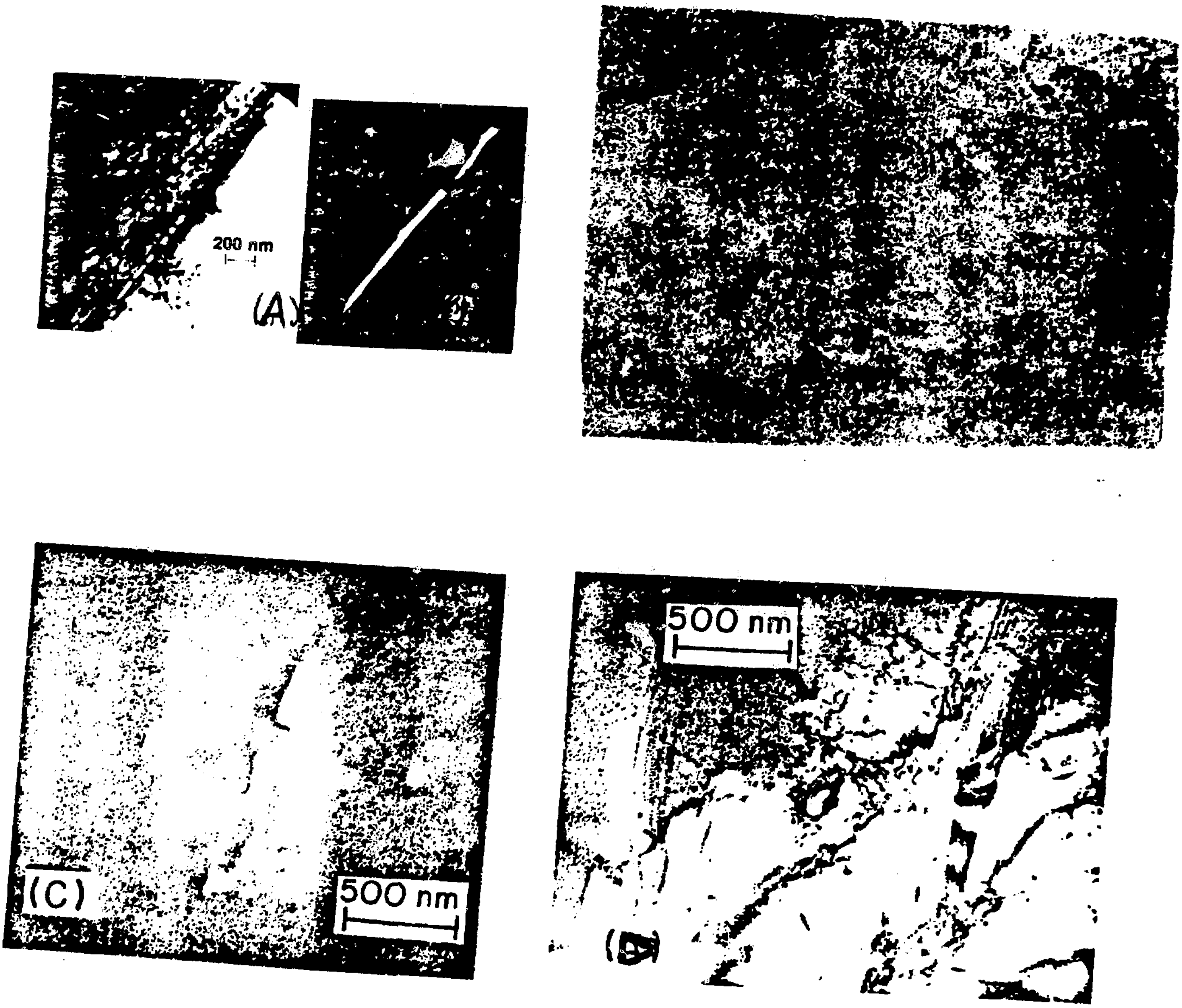

Fig. 3. Morphology of $M_{23}C_6$ Carbides in Aged CF-8 and CF-8M Steels. (A) KRB reactor pump; (B) heat 278, aged at 400°C for 70,000 h; (C) heat 286, aged at 400°C for 10,000 h; and (D) bright-field of (C).

④

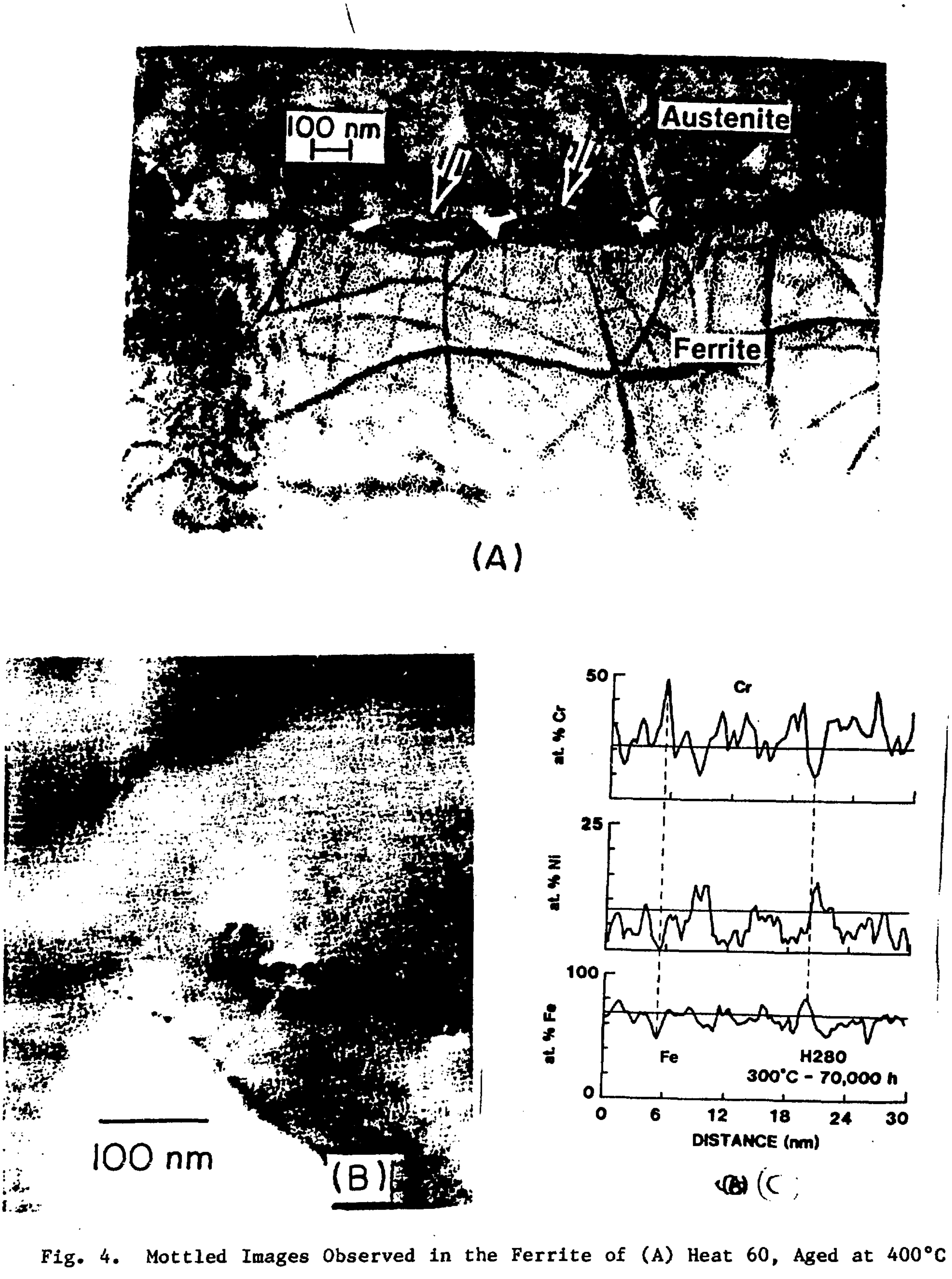

Fig. 4. Mottled Images Observed in the Ferrite of (A) Heat 60, Aged at 400°C for 10,000 h; (B) Heat 280, Aged at 300°C for 70,000 h; and (C) APFIM Profiles of Cr, Ni, and Fe in the Ferrite of (B).

5

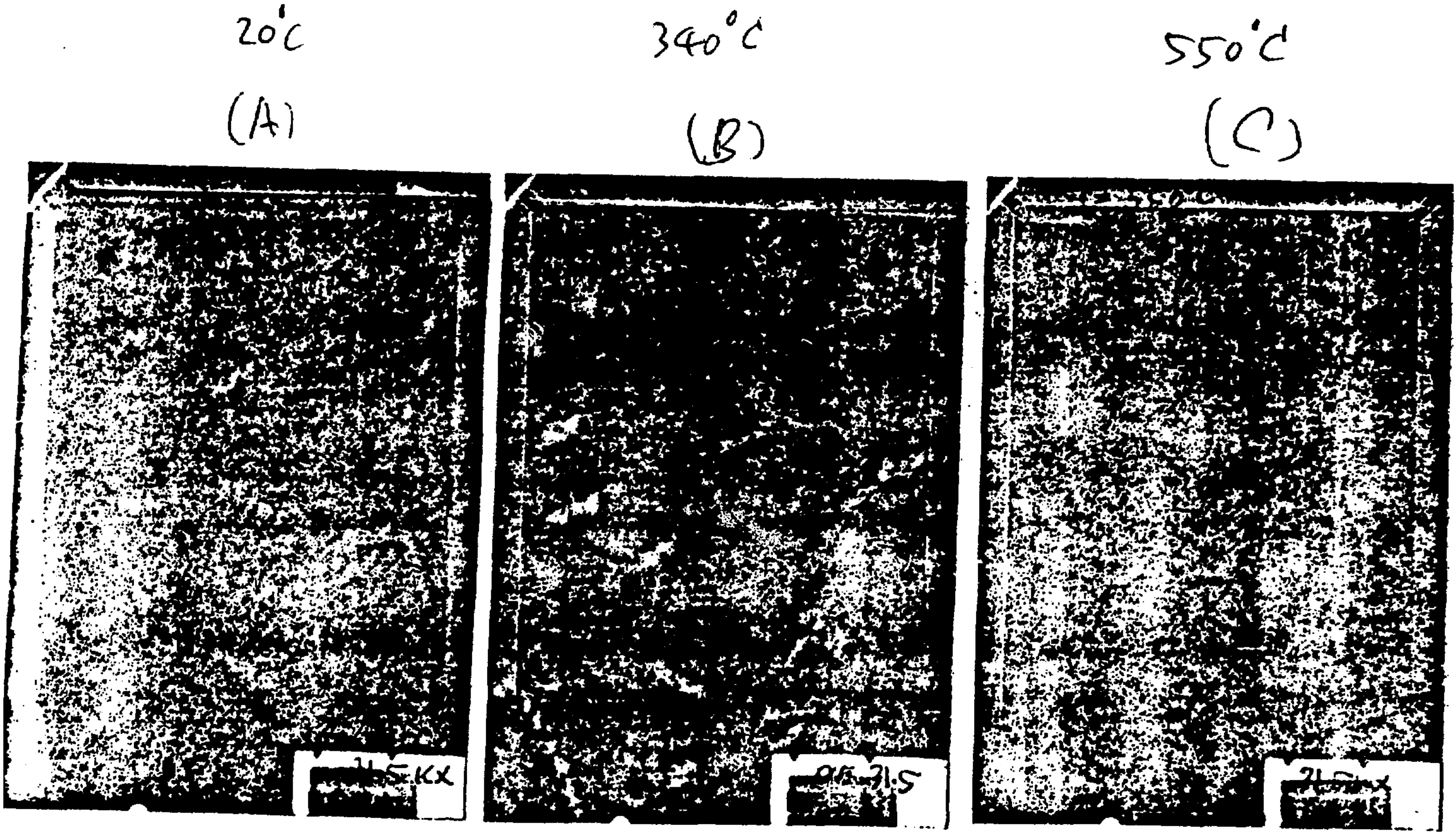

Fig. 5. Morphology of the Large Platelike α' Observed in Heat 280N (Aged at 350°C for 56,000 h) During Heating in the HVEM Hot Stage, (A) 20°C; (B) 340°C; and (C) 550°C.

5

⑥

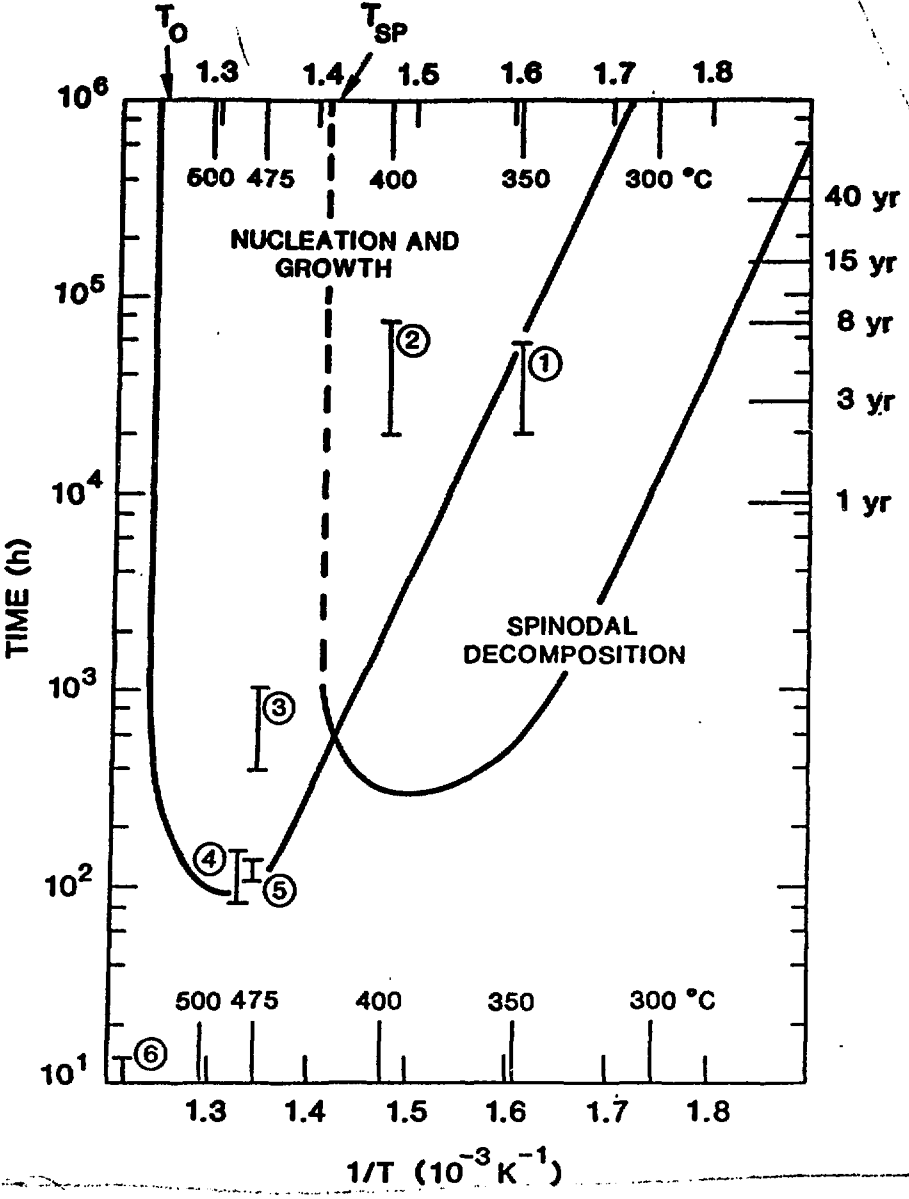

New

Fig. 6. Arrhenius Plot of the Precipitation of the Large Platelike α'. For comparison, regions of spinodal decomposition and α' precipitation by nucleation and growth are shown. Slopes of the linear portions represent an activation energy of ~48 kcal/mol. Data denoted by numbers 1 to 6 represent results from (1) heat 280N, this study; (2) heat 280, this study; (3) 29Cr-4Mo-2Ni ferritic steel, this study; (4) 21Cr steel, Blackburn and Nutting;[18] (5) Heat U50 Duplex Steel, Solomon and Levinson;[20] and (6) 30Cr steel, Lagneborg.[17]

⑦

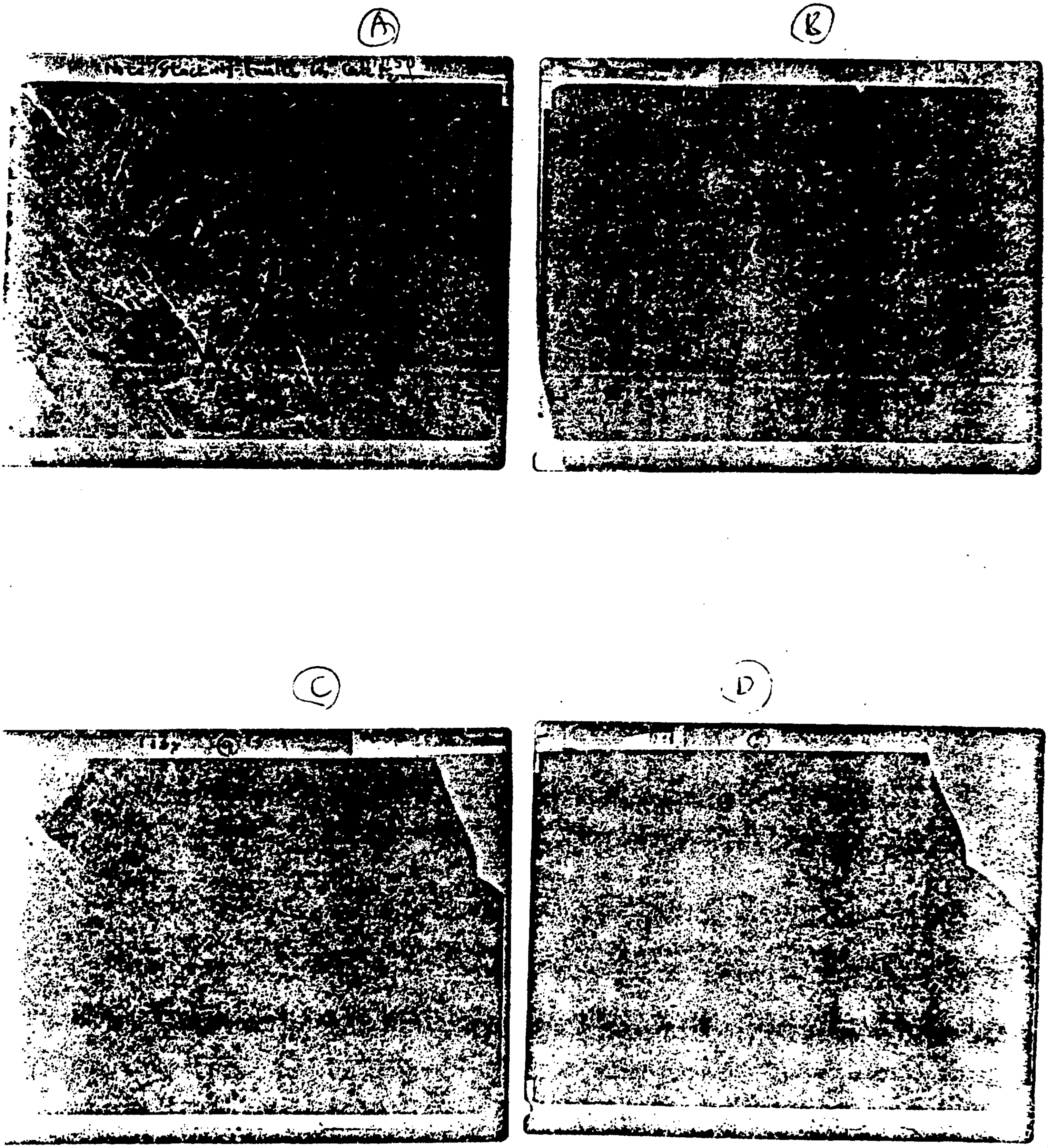

Fig. 7. Morphology of γ_2 Precipitates in Ferrite. (A) Bright-field image of a region of ferrite containing the γ_2 in heat 278, aged 400°C for 70,000 h; (B) SAD pattern of (A); dark-field images of (C) γ_2; and (D) ferrite. Note streaks in γ_2 reflections in (B).

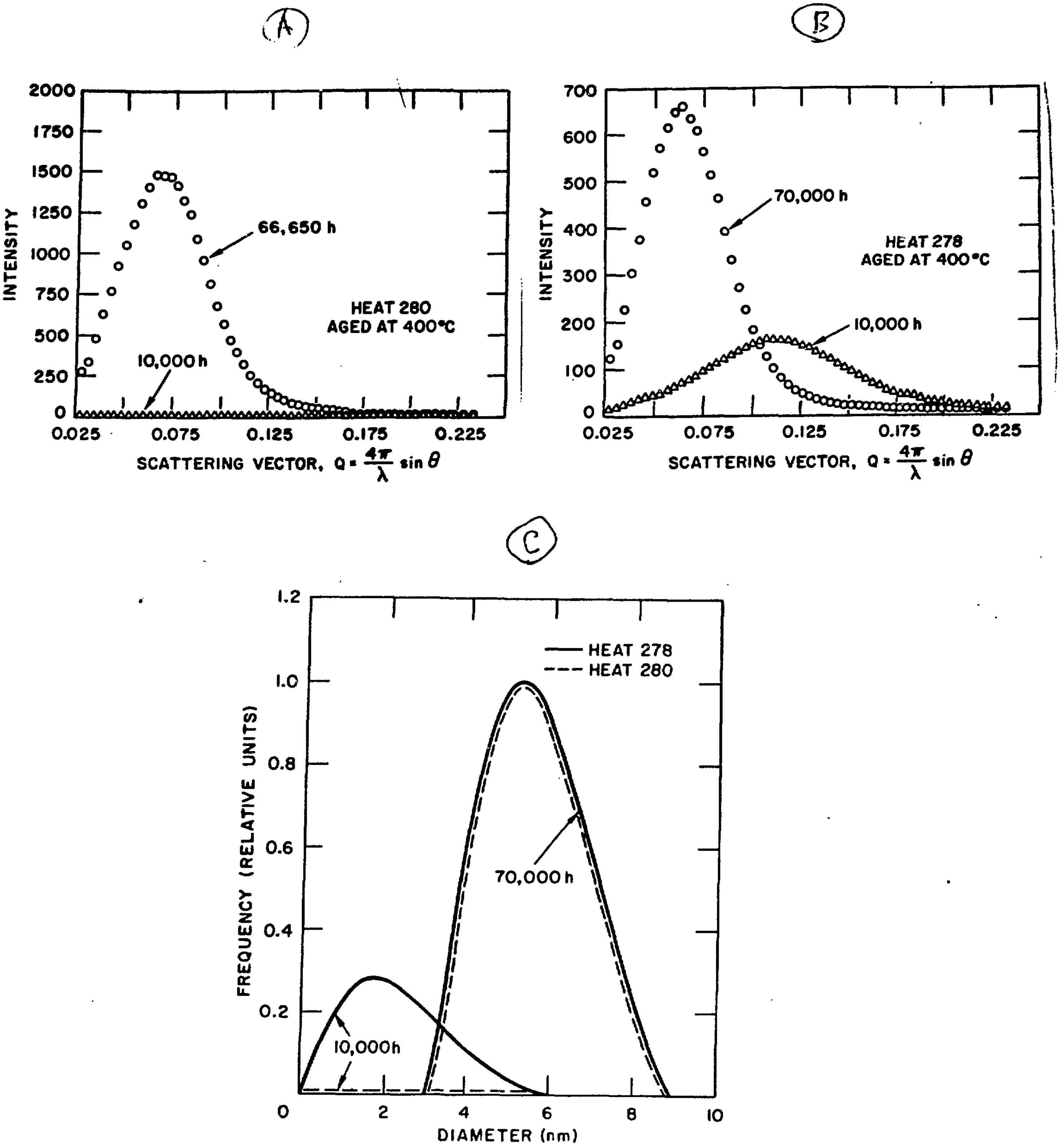

Fig. 8. SANS Characteristics of Long-Term-Aged Cast Duplex Stainless Steels. (A) Heat 280, aged at 400°C for 10,000 and 66,650 h; (B) heat 278, aged at 400°C for 10,000 and 70,000 h; (C) size distribution of precipitates obtained by Guinier transformation of (A) and (B).

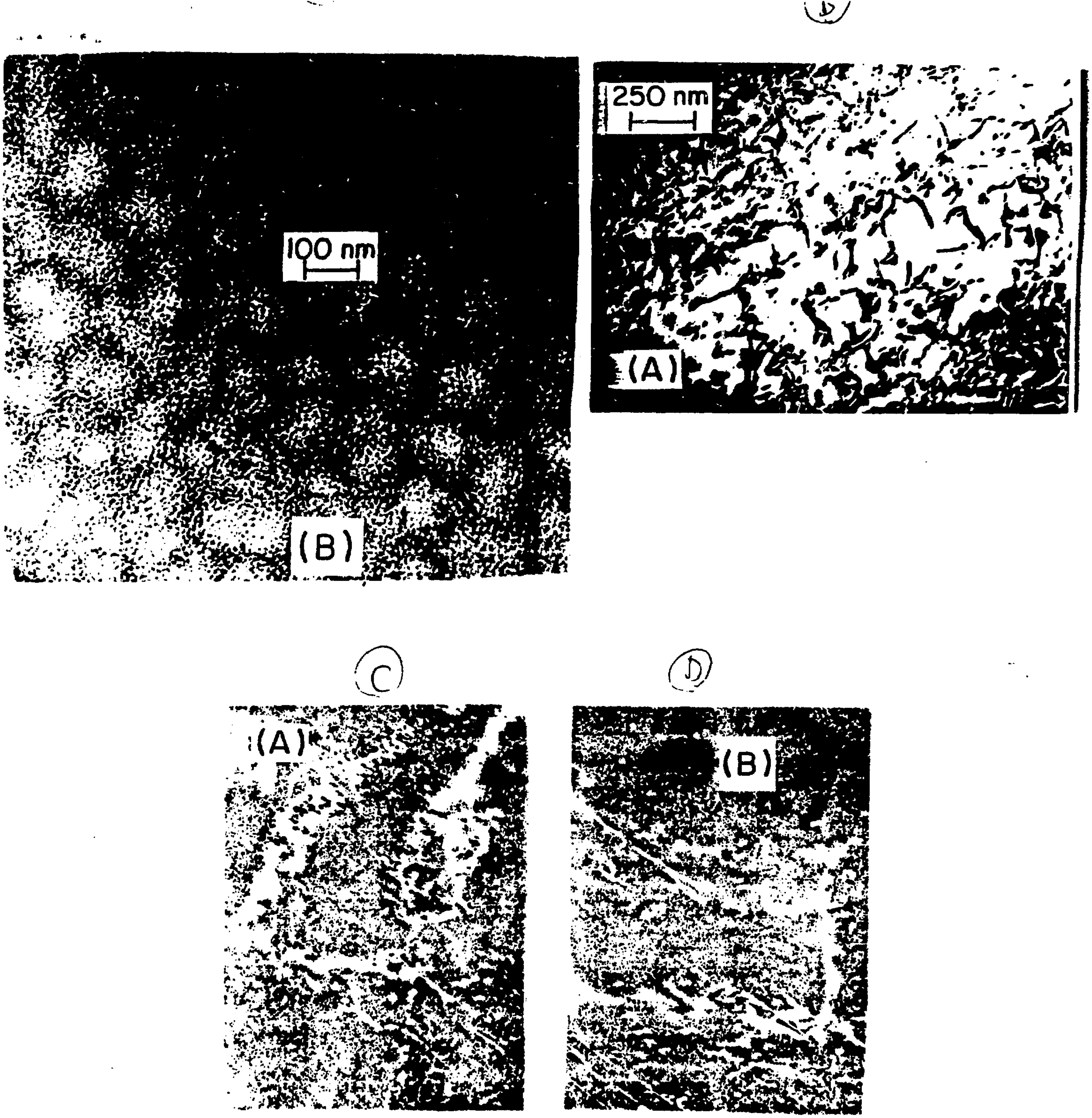

Fig. 9. Microstructural Evolution of the Ferrite Phase of Long-Term-Aged Specimens after Annealing at 550°C for 1 h. (A) Spinodal decomposition in ferrite of the KRB pump cover after ~12 yr service; (B) ferrite of (A) after the 550°C anneal showing dissolution of the Cr-rich regions of spinodal decomposition and a high density of dislocations after impact test; (C) G-phase precipitates in the ferrite of heat 280 after aging at 400°C for 70,000 h; and (D) same region as (C) after the 550°C annealing.

⑩

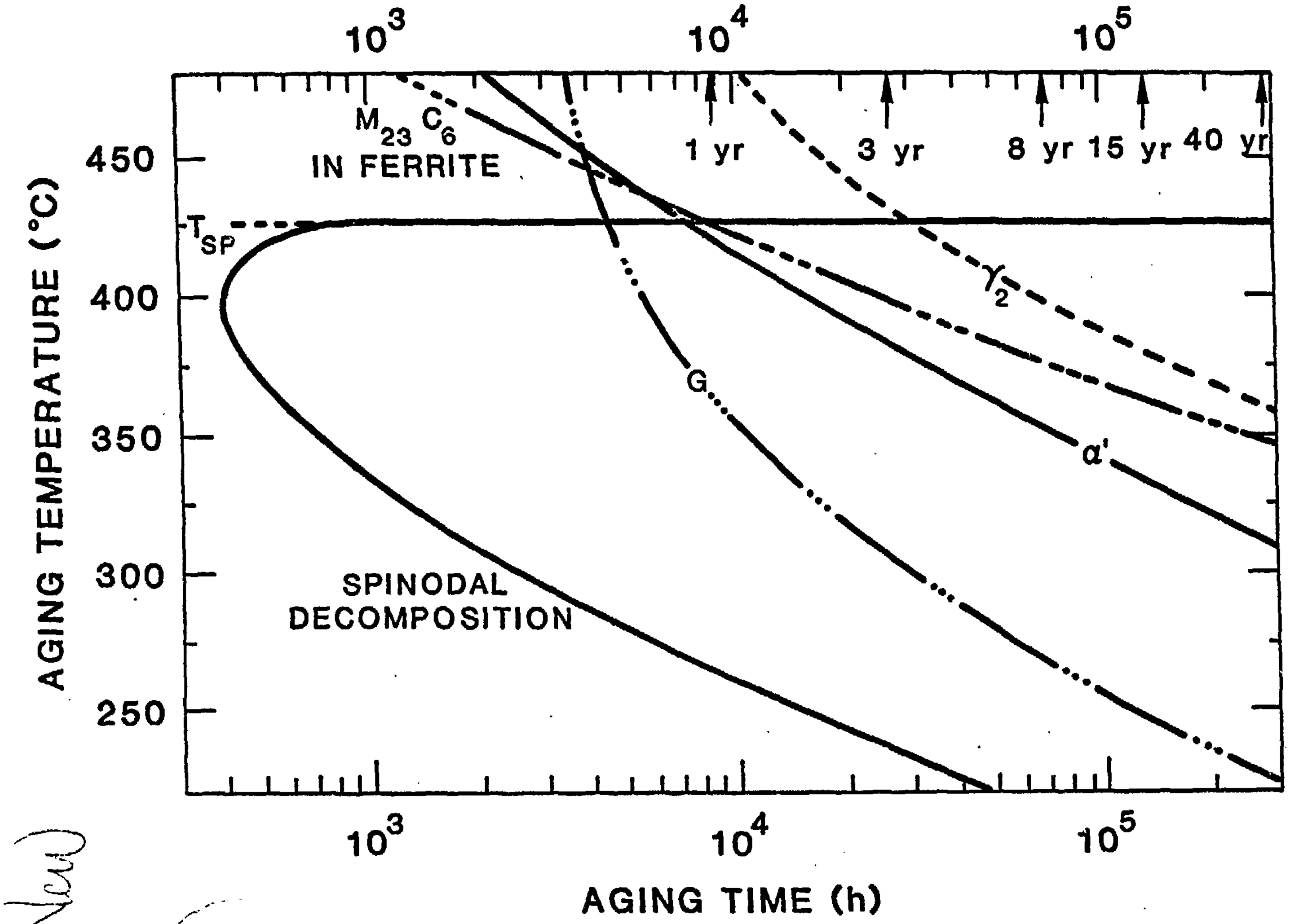

New

Fig. 10. Approximate TTT Diagrams for the Precipitation of the G, γ_2, $M_{23}C_6$, α', and Spinodal Decomposition in Ferrite of Cast Duplex Stainless Steels for Aging Temperatures 250-450°C.